J Mater Sci (2009) 44:5102–5112
DOI 10.1007/s10853-009-3545-1

FERROELECTRICS

Crystal chemistry and domain structure of rare-earth doped $BiFeO_3$ ceramics

S. Karimi · I. M. Reaney · Y. Han · J. Pokorny · I. Sterianou

Received: 7 April 2009 / Accepted: 4 May 2009 / Published online: 9 June 2009

Abstract $Bi_{(1-x)}RE_xFeO_3$ (BREF100x, RE = La, Nd, Sm, Gd) has been investigated with a view to establish a broad overview of their crystal chemistry and domain structure. For $x \leq 0.1$, the perovskite phase in all compositions could be indexed according to the rhombohedral, R3c cell of $BiFeO_3$. For Nd and Sm doped compositions with $0.1 < x \leq 0.2$ and $x = 0.15$, respectively, a new antipolar phase was stabilised similar in structure to $PbZrO_3$. The orthoferrite, Pnma structure was present for $x > 0.1$, $x > 0.15$, and $x > 0.2$ in Gd, Sm, and Nd doped $BiFeO_3$, respectively. For $x > 0.2$, La doped compositions became pseudocubic at room temperatures but high angle XRD peaks were broad and asymmetric. These compositions have been indexed as the orthoferrite structure. It was concluded therefore that the orthoferrite phase appeared at lower values of x as the RE ferrite, end member tolerance factor decreased. However, the compositional window over which the $PbZrO_3$-like phase was stable increased with increasing end member tolerance factor but was not found as single phase in La doped compositions at room temperature. On heating, the $PbZrO_3$-like phase in BNF20 transformed to the orthoferrite, Pnma structure. T_C for all compositions decreased with decreasing A-site, average ionic polarizabilty and tolerance factor. For compositions with R3c symmetry, superstructure and orientational, and translational (antiphase) domains were observed in a manner typical of an antiphase-tilted, ferroelectric perovskite. For the new $PbZrO_3$-like phase orientational domains were observed.

S. Karimi · I. M. Reaney (✉) · Y. Han · J. Pokorny · I. Sterianou
Department of Engineering Materials, University of Sheffield, Sheffield S1 3JD, UK
e-mail: i.m.reaney@sheffield.ac.uk

Introduction

$BiFeO_3$ is reported to be a rhombohedrally distorted perovskite with space group R3c at room temperature in which the Bi^{3+} ions occupy the cubo-octahedral positions and Fe^{3+} ions in octahedral coordination. The cations displace off their centre of symmetry along $[111]_p$ direction with the anion sublattice distorted according to an $a^-a^-a^-$ tilt system in which the FeO_6 octahedra are rotated in antiphase around the rhombohedral axis. The Bi^{3+} ions have larger displacement compared to the Fe^{3+}, due to the active lone pair electron and this, results in O ions being effectively fourfold coordinated to two Bi^{3+} ions and two Fe^{3+} ions [1, 2].

$BiFeO_3$ is ferroelectric below 830 °C but does not exhibit a saturated polarisation versus electric field loop at room temperature due to a combination of the high Curie Temperature (T_C) and conductivity. However, based on the theoretical calculations, the spontaneous polarisation is expected to be high due to the large displacements of the cations [3–5]. Magnetic susceptibility measurements have indicated that $BiFeO_3$ is antiferromagnetic below the Neel temperature, $T_N = 370$ °C. High resolution neutron diffraction studies have shown that the magnetic order of $BiFeO_3$ is not completely described by NaCl, G-type ordering but rather follows a cycloidal spiral in the $[110]_h$ direction with a period, $\lambda = 620$ Å within a $(110)_h$ spin rotation plane. Such complex magnetic order is unusual for ferrites with the perovskite structure and the presence of a space modulated spin structure is considered to inhibit the linear magnetoelectric effect [6–8].

Despite these limitations, $BiFeO_3$ has gained great attention in recent years because of the coexistence of ferroelectric and antiferromagnetic ordering and is considered to have tremendous potential for applications in the

field of information storage, sensing, and actuation, e.g., multiple state memory elements, electric field controlled ferromagnetic resonance devices, and transducers with magnetically modulated piezoelectricity [9–11]. To promote a strong magnetoelectric effect, a ceramic or thin film should exhibit low-leakage current, long range ferroelectric order, and display large remnant magnetization [12, 13]. To meet these criteria, researchers have turned their attention to the use of dopant and substituent ions [12–21].

Partial substitution of Bi^{3+} ions by lanthanides has been shown to improve ferroelectric properties and magnetization [9, 14, 18, 19]. Das et al. [19] and Zhang et al. [14] suggested that La^{3+} substitution for Bi^{3+} eliminates impurity phases and destroys the cycloidal spin structure resulting in uniform canted antiferromagnetic ordering. Zhang et al. [14] also reported that the structure changes from rhombohedral to orthorhombic at ~30 mol% La. Yuan et al. [12], in their investigations of Sm and Nd [20] doped $BiFeO_3$, reported a change in the crystal structure of the material which resulted in improved piezoelectric properties, long-range ferroelectric and canted anti-ferromagnetic orders. Uniyal et al. [21] claimed that 10 mol% Gd substituted for bismuth did not change the crystal structure but reduced the volume fraction of impurity phases, decreased T_N to ~150 °C, increased magnetization and allowed ferroelectric hysteresis loops to be generated [21].

Comparisons with other systems, such as $Pb(Zr,Ti)O_3$, are potentially useful for predicting the behaviour of $BiFeO_3$ as a function of increasing RE concentration. Figure 1 shows the PZT phase diagram. In the R phase field, as the larger, less polarisable Zr^{4+} substitutes for Ti^{4+} ions, the tolerance factor (t) and ferroelectric T_C decrease,

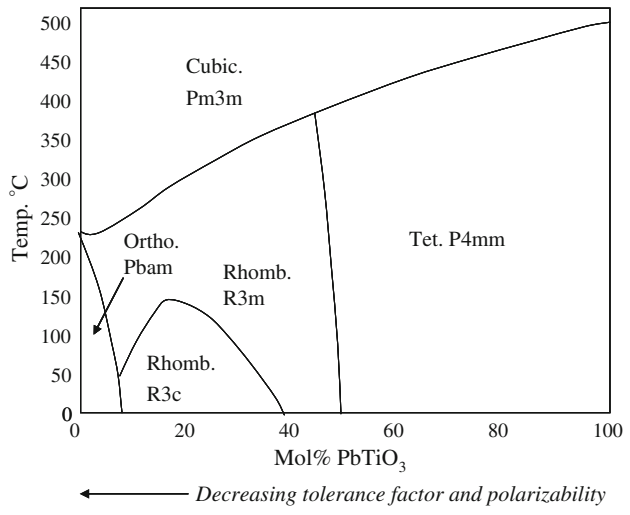

Fig. 1 $Pb(Zr_{1-x}Ti_x)O_3$ phase diagram [23]

Table 1 Tolerance factor and space groups of bismuth and RE ferrites [24]

Composition	$BiFeO_3$	$LaFeO_3$	$PrFeO_3$	$NdFeO_3$	$SmFeO_3$	$GdFeO_3$
Tolerance factor	0.96	0.95	0.94	0.93	0.92	0.91
Symmetry	R3c	Pnma	Pnma	Pnma	Pnma	Pnma

$$t = (R_A + R_O)/\sqrt{2}(R_B + R_O),$$

where R_A, R_B, and R_O are the ionic radii of the A, B, and O sites. As t decreases, the driving force for octahedral rotation increases [2, 22, 23], initially resulting in a transition from R3m to R3c but ultimately transforming the structure to the antiferroelectric, *Pbam* phase. Table 1 shows the tolerance factor and space group symmetries of the end members for several $BiFeO_3$–$REFeO_3$ solid solutions. For all RE dopants therefore, there is a decrease in tolerance factor [24] as concentration increases and additionally the polarizabity of the A-site decreases [25]. By analogy with PZT, there is a strong likelihood of a transition from polar to antipolar order in these systems. The observation of an antiferroelectric, $PbZrO_3$-like phase has already been reported for Nd doped $BiFeO_3$ but to date this is the only observation of antipolar order in bulk RE-doped $BiFeO_3$ [26]. More trivially, as RE concentration increases, the solid solution will favour the orthoferrite ($a^-a^-c^+$, *Pnma*) rather than rhombohedral ($a^-a^-a^-$, *R3c*) structure [27].

The above brief summary highlights the need for a concise overview of the substitution of RE dopants for Bi in $BiFeO_3$. Here, we investigate a broad range of RE dopants with a view to establish the generic trends in crystal chemistry and determine the domain structure.

Experimental

Compositions with the $(Bi_{1-x}RE_x)FeO_3$ and RE = La, Nd, Sm, or Gd $0 \leq x \leq 0.4$ formula were produced using high-purity (>99%) Bi_2O_3, Fe_2O_3, La_2O_3, Nd_2O_3, Sm_2O_3, and Gd_2O_3. Stoichiometric batches of raw materials were attrition-milled in propan-2-ol for 1 h, using 3 mm diameter yttria-stabilized zirconia media. The resultant slurry was dried at ~80 °C, crushed with agate pestle and mortar and passed through a 355 μm sieve. $BiFeO_3$ powder was reacted at 830 °C and doped compositions at 870 °C for 3 h in lidded alumina crucibles and then milled and dried as above. Pellets were pressed in a 10 mm die at ~250 MPa and sintered for 3 h in air at 870 °C for $BiFeO_3$ and 920 °C for doped samples. Sintered pellets exhibited a density >95% theoretical. All

samples were examined by scanning electron microscopy which indicated a typical grain size of 5–10 μm for all compositions.

Differential Scanning Calorimetry (DSC) was carried out using a NETZSCH DSC 404 C. Measurements were carried out from 20 °C up to 850 °C with a heating rate of 20 °C min^{-1}. X-ray diffraction (XRD, Siemens D500) was used primarily to identify the phase assemblage of the samples. The diffracted intensity across the 2θ-range of 20°–70° was measured in steps of 0.02° at a speed of 1° per minute. A transmission electron microscope (TEM, Philips EM420T) operating at 120 kV was used to obtain microstructural data of the grain and domain morphologies and electron diffraction patterns from principal zone axes. Unpolarised Raman spectra were excited with the 514.5 nm line of an Ar laser and recorded in back scattering geometry using a Renishaw InVia micro-Raman spectrometer. Laser power of 4 mW was focused on a ~2 μm spot. The spectral resolution was ~1 cm^{-1}.

Results

X-ray diffraction

Figure 2 shows the XRD patterns for sintered pellets for $(Bi_{1-x}RE_x)FeO_3$ and RE = La, Nd, Sm, or Gd with $0 \leq x \leq 0.4$. Generally, for $x < 0.1$ second phase peaks attributed to Bi or Fe rich phases, $Bi_2Fe_4O_9$ and $Bi_{25}FeO_{40}$ are routinely observed. However, for $x \geq 0.1$, all peaks in the XRD traces are related to perovskite-structured phases. For La doped compositions with $x \leq 0.2$, all major peaks may be indexed according to the R3c cell of the $BiFeO_3$ structure. For La doped compositions with $x > 0.2$, the peaks are pseudocubic with no peak splitting within the resolution limit of the *in-house* diffractometer. However, significant broadening of, e.g., the $(202)_p$ and $(310)_p$, peaks suggest a distortion away from cubic, possibly arising from the orthoferrite structure, used to index this XRD trace. For Nd and Sm doped $BiFeO_3$ with $x < 0.15$, all peaks are

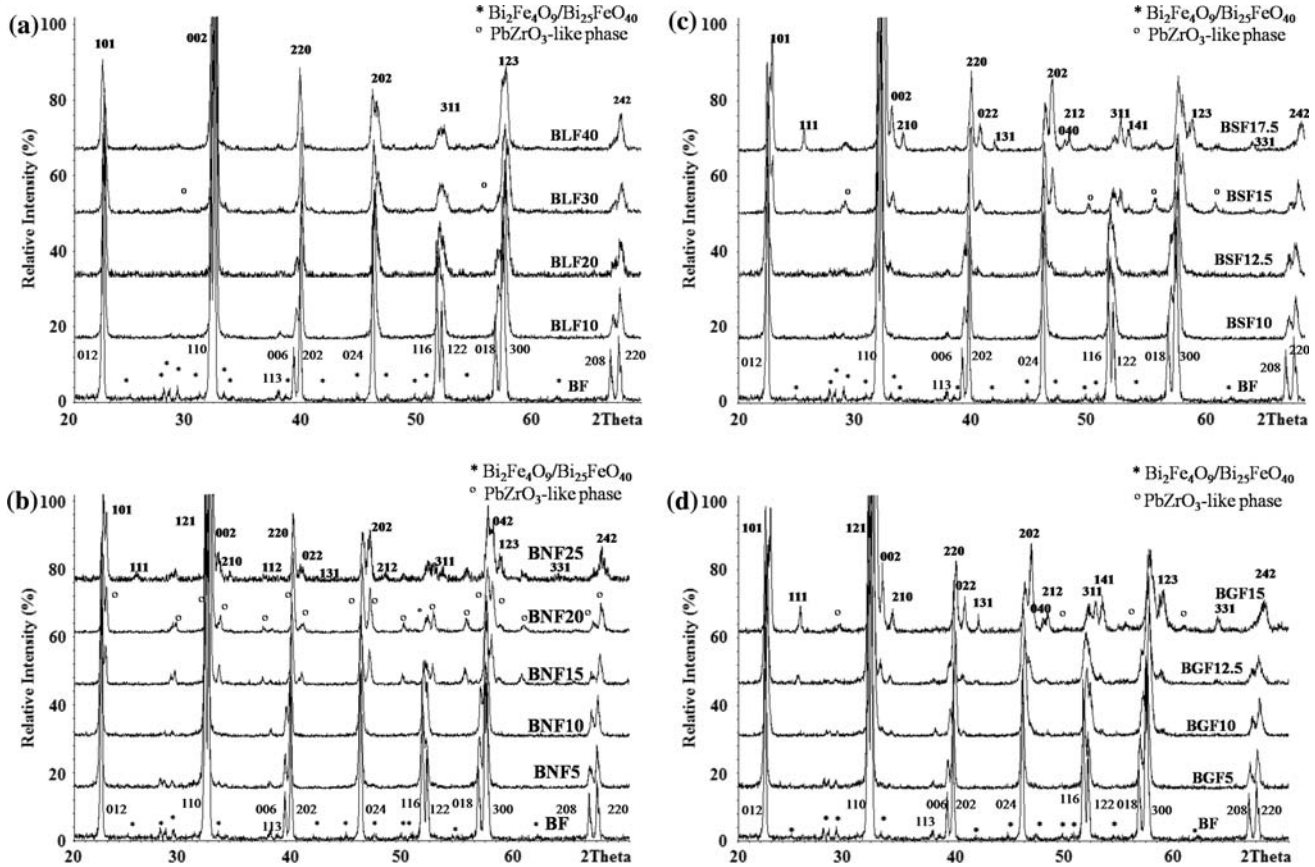

Fig. 2 XRD patterns for $(Bi_{1-x}RE_x)FeO_3$ where RE = **a** La, **b** Nd, **c** Sm, and **d** Gd $0 \leq x \leq 0.4$. $BiFeO_3$ is indexed according the *R3c* space group, BSF15 and BNF15/20 according to the $PbZrO_3$ structure and BLF30, BLF40, BNF25, BSF17.5, and BGF15 are indexed according the orthoferrite (*Pnma*) structure

indexed according to the R3c cell of $BiFeO_3$. However, for BNF15 and BSF15 a new phase appears whose peaks can be indexed according to an orthorhombic $PbZrO_3$-structure [26]. The $PbZrO_3$-phase is retained for BNF20, but for BSF17.5 and BNF25 the major peaks are indexed according to the orthoferrite structure [26] although some peaks attributed to the new $PbZrO_3$ phase are also present. For Gd and La doped compositions, some peaks in ceramics with $x = 0.15$ and $x = 0.3$, respectively, can be attributed to the new $PbZrO_3$-like structure but single phase is not observed at room temperature.

The comparison of the new BNF15/BNF20/BSF15 phase with $PbZrO_3$ is shown in Fig. 3. The traces do not overlap since the fundamental pseudocubic lattice of $PbZrO_3$ (~4.1 Å) is much larger than that of $BiFeO_3$ (~3.9 Å) but the strong similarity of the traces clearly indicates that the distortions of the cation sublattices in BNF15/BNF20/BSF15 are virtually identical to $PbZrO_3$. Preliminary Rietveld refinements for Nd doped samples, using XRD data have been presented elsewhere but they are consistent with the idea that Bi displacements adopt the same antipolar arrangements as observed for Pb in the antiferroelectric $PbZrO_3$ structure [26]. $PbZrO_3$ is the archetype antiferroelectric perovskite in which the orthorhombic unit cell may be described on a $\sqrt{2}a$, $2\sqrt{2}a$, $2a$ matrix with the c axis coincident with the fundamental perovskite lattice but with a and b rotated through 45°. The structural distortions within the cell may be envisaged as antipolar displacements of the Pb ions along $[110]/[-1-10]_p$ direction and antiphase rotations of the O-octahedra described by an $a^-a^-c^0$ tilt system. In combination these two structural distortions give rise to Pbam symmetry [28]. For Sm doped compositions, only BSF15 exhibits the $PbZrO_3$ phase whereas BSF17.5 is best described by the orthoferrite structure, Pnma, $a^-a^-c^+$ [27]. In contrast, in Nd doped samples the phase field of existence of the $PbZrO_3$ phase is ≥5 mol%.

Differential scanning calorimetry

T_C obtained from DSC for samples where reliable peaks could be detected are shown in Table 2 along with the average A-site polarizability and tolerance factor for each composition. A typical set of DSC traces for Nd doped $BiFeO_3$ samples is shown in Fig. 4. For undoped $BiFeO_3$ a

Table 2 T_C, average tolerance factor [24] and average A-site polarizability [25] for BREF100x (NB: only data are recorded for composition where T_C could be reliably determined)

Composition	Average A-site polaris (Å^3)	Average tolerance factor	T_C (°C)
BF	6.12	0.96429	830
BLF5	6.118	0.96375	754
BLF10	6.115	0.96321	677
BNF5	6.0645	0.96286	696
BNF10	6.009	0.96143	518
BNF15	5.9535	0.96	325
BNF20	5.898	0.95857	170
BSF5	6.051	0.96232	677
BSF10	5.982	0.96036	448
BSF15	5.913	0.9584	309
BGF05	6.0325	0.962	652
BGF10	5.945	0.959	372

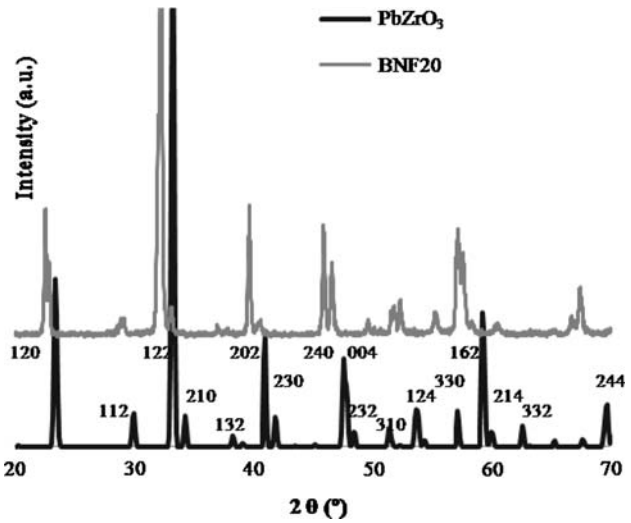

Fig. 3 Comparison of experimental XRD traces from BNF20 with $PbZrO_3$ indexed according to the *Pbam* $PbZrO_3$ cell

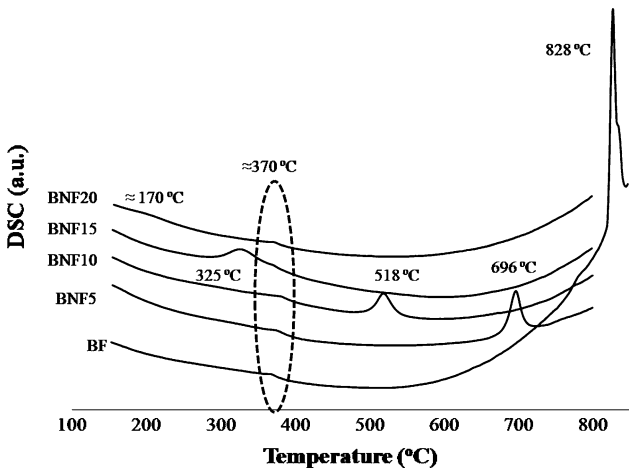

Fig. 4 DSC curves for $(Bi_{1-x}RE_x)FeO_3$ and RE = La, Nd, Sm, and Gd

strong peak is observed at 828 °C consistent with the reported T_C. However, a weak anomaly is also observed at ~750 °C. The origin of this peak is unknown and it may indicate a further structural phase transition in undoped $BiFeO_3$ or be related to second phase (Fig. 4). For La doped samples with $x = 0.05$ and 0.1, peaks attributed to a ferroelectric T_C were observed at 754 and 677 °C, respectively. For compositions with $x > 0.1$, there are no further sharp anomalies. Changes in the gradient of the DSC curves were, however, apparent at lower temperatures suggesting broad phase transition. Similar trends are observed in Sm and Gd doped compositions. Strong anomalies corresponding to T_C are observed for $x \leq 0.1$ with only deviations in the gradient of the DSC curve apparent for higher concentrations. This effect is attributed to the heterogeneous distribution of the RE ion. For Nd doped ceramics, however, a strong peak is also observed for BNF15 at ~325 °C (Fig. 4). Significantly, a broad anomaly is observed in all RE doped compositions at ~370 °C (Fig. 4), which has been reported as T_N for $BiFeO_3$ [6–8].

Figure 5 shows a plot of T_C versus x for Nd doped compositions. For BNF20, the phase transition has been taken as ~170 °C, the mid-point of the deviation in gradient around that temperature. As expected, the relationship is linear and T_C decreases with increasing x. Figures 6 and 7 are plots of average tolerance factor [24] and average A-site polarizability, [25] respectively, versus T_C for all compositions. As average tolerance factor and A-site ionic polarizability decrease, T_C decreases. However, across the Lanthanide series, ionic polarizability is directly proportional to ionic radius and therefore it is difficult to distinguish which of the two crystallochemical factors is most important in controlling T_C in RE doped $BiFeO_3$.

Transmission electron microscopy

To further study the domain and crystal structure of RE doped $BiFeO_3$, TEM samples were prepared for several key compositions. Figure 8 shows the $\langle 110 \rangle_p$ zone axis electron diffraction patterns for BNF10. Identical patterns were obtained for all compounds with $x \leq 0.1$. As anticipated, $\frac{1}{2}\{ooo\}_p$ superstructure reflections are present that arise from antiphase rotation of the octahedra around the $[111]_p$ axis. For an $a^-a^-a^-$ tilt system, 6/12 $\langle 110 \rangle_p$ zone axes are expected to contain $\frac{1}{2}\{ooo\}_p$ reflection [29]. Figure 9a and b are bright and dark field images of parts of a grain in BNF10 which show the orientational and translational domain structures. Figure 9a illustrates a typical non-180° domain wall arising from the ferroelectric/ferroelastic distortion of the lattice. Figure 9b was obtained under two beam conditions utilising a $\frac{1}{2}\{ooo\}_p$ reflection and the planar defects are antiphase boundaries where regions of antiphase tilt impinge out of phase.

Figure 10 shows a $\langle 001 \rangle_p$ zone axis diffraction patterns obtained from BNF20. Identical patterns could, however, be obtained from BNF15 and BSF15. These patterns, first reported in Ref. [26], illustrate that the $PbZrO_3$-like phase identified by XRD is not only quadrupled along one of the $\langle 110 \rangle_p$ directions (i.e., a periodicity of $2\sqrt{2}a$) giving rise to

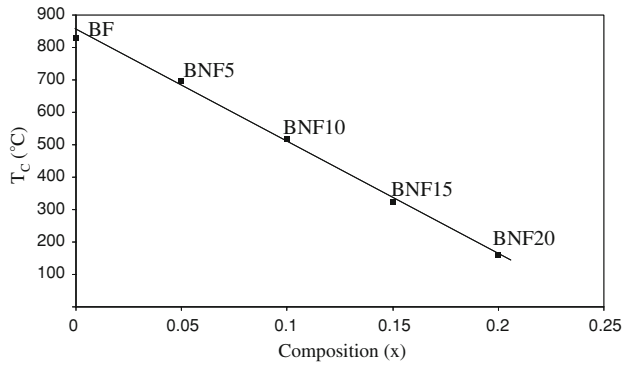

Fig. 5 Plot of T_C versus concentration (x) for BNF100x

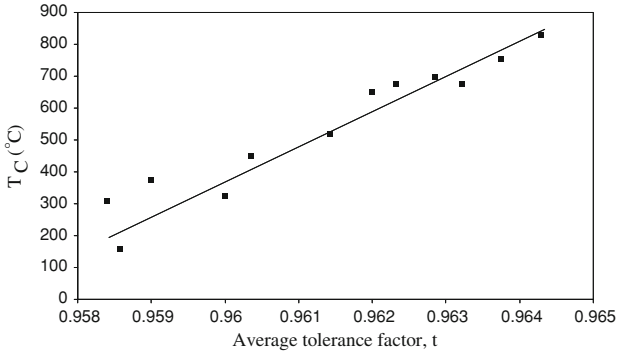

Fig. 6 Plot of T_C versus tolerance factor for all compositions where DSC reliably indicates a phase transition

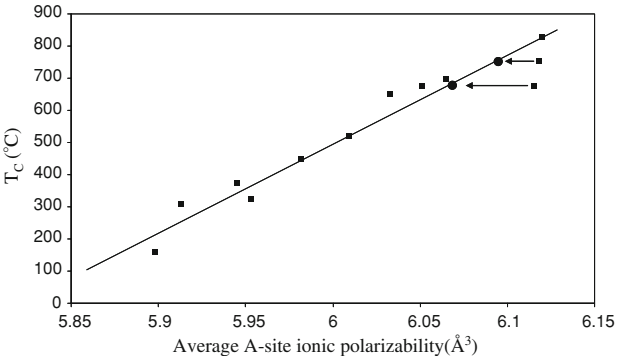

Fig. 7 Plot of average A-site ionic polarizability for all compositions where DSC reliably indicates a phase transition. Data points using a modified polarizability for La^{3+} ~5.5 Å^3 are arrowed

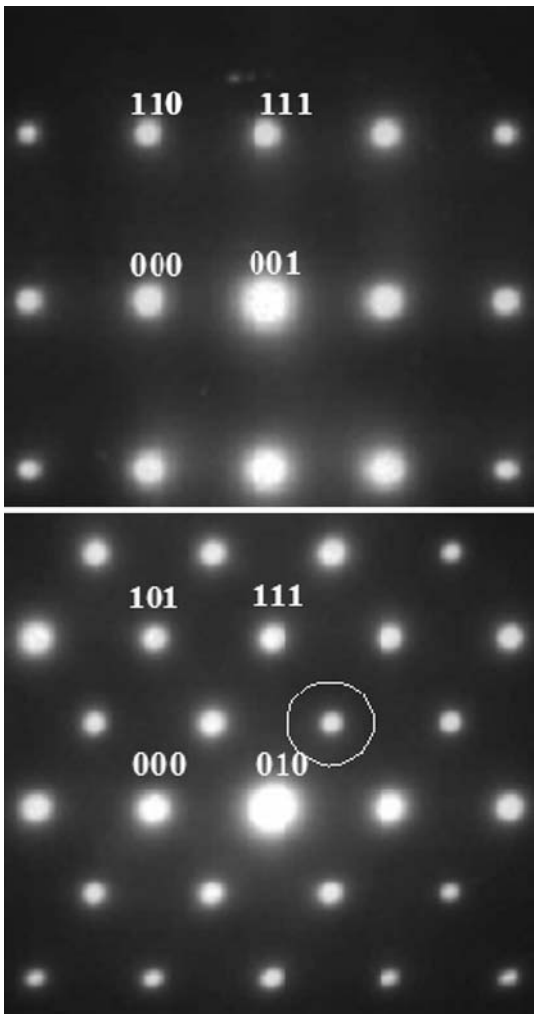

Fig. 8 Electron diffraction patterns from two variants of the $\langle 110 \rangle_p$, zone axes in BNF10. Superstructure reflections associated with antiphase rotations of the *O*-octahedra are ringed

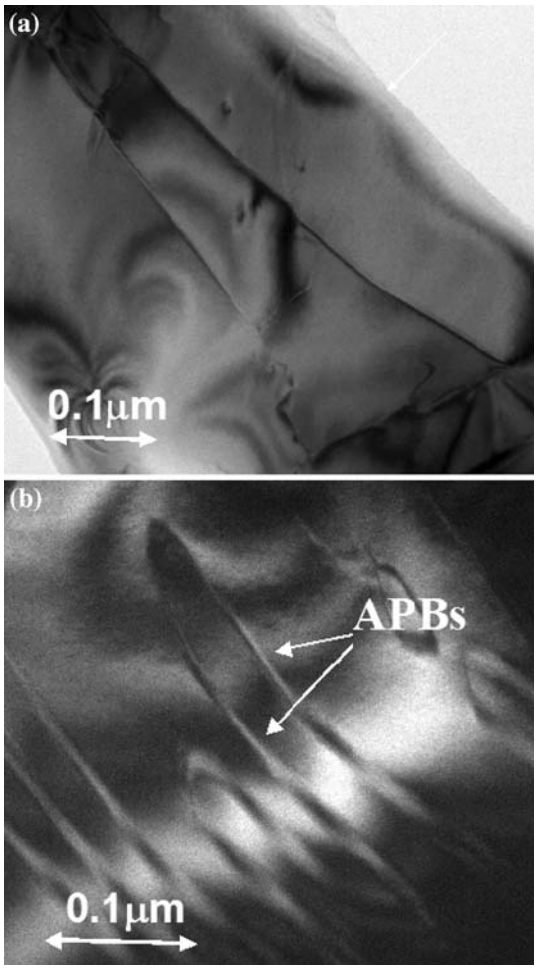

Fig. 9 **a** Bright field and **b** dark field images of orientational and translational domains in BNF10. Figure 9b was obtained with the electron beam parallel with a $\langle 110 \rangle_p$, utilising a $1/2\{ooo\}_p$ superstructure reflection under two beam conditions

¼$\{hk0\}_p$ reflections but also along the $\langle 001 \rangle_p$, manifested as the appearance of ¼$\{00l\}_p$ reflections. Superstructure reflections at ½$\{ooo\}_p$ positions associated with antiphase rotations of the [FeO_6] octahedra were also present. The unit cell which best fits the ED data is similar to that of $PbZrO_3$ ($\sqrt{2}a$, $2\sqrt{2}a$, $2a$) except that the c axis is quadrupled rather than doubled with respect to the fundamental perovskite lattice, a, giving a unit cell which is approximately, $\sqrt{2}a,2\sqrt{2}a,4a$. The precise nuclear and magnetic structure of this phase will be reported elsewhere. Figure 11 is a dark field image illustrating the ferroelastic domain structure in a grain of BNF20 with the electron beam parallel with $\langle 110 \rangle_p$. The image was obtained using a ½$\{ooo\}_p$ reflection (ringed). Adjacent to the image are the three domain variants of the pseudocubic $\langle 110 \rangle_p$ obtained from each highlighted domain.

Figure 12 shows a bright field image of a region in BGF15 obtained at room temperature. The grain contains a mixture of $PbZrO_3$-like and orthoferrite phase, consistent with XRD data shown in Fig. 2. This gives rise to a highly complex domain structure. Inset are [001] zones axes from each phase. The quadrupled reflections of the $PbZrO_3$-like phase are arrowed and ½{eeo} reflections of the orthoferrite phase are ringed.

Figure 13 shows in situ electron diffraction data obtained from BNF20. As temperature increases, ¼$\{hk0\}_p$ reflections are replaced by ½$\{ooe\}_p$ and the ¼$\{00l\}_p$ reflections by ½$\{eeo\}$. The transition temperature is broad consistent with the wide peak in the DSC trace for this composition. The appearance of ½$\{ooe\}_p$ and ½$\{eeo\}_p$ superstructure reflections indicate the presence of in-phase tilting in perovskite structured compounds [30]. Further zone axis electron diffraction patterns from the high temperature phase were all consistent with an $a^-a^-c^+$ tilt system which gives rise to *Pnma* symmetry, identical to the orthoferrite end member.

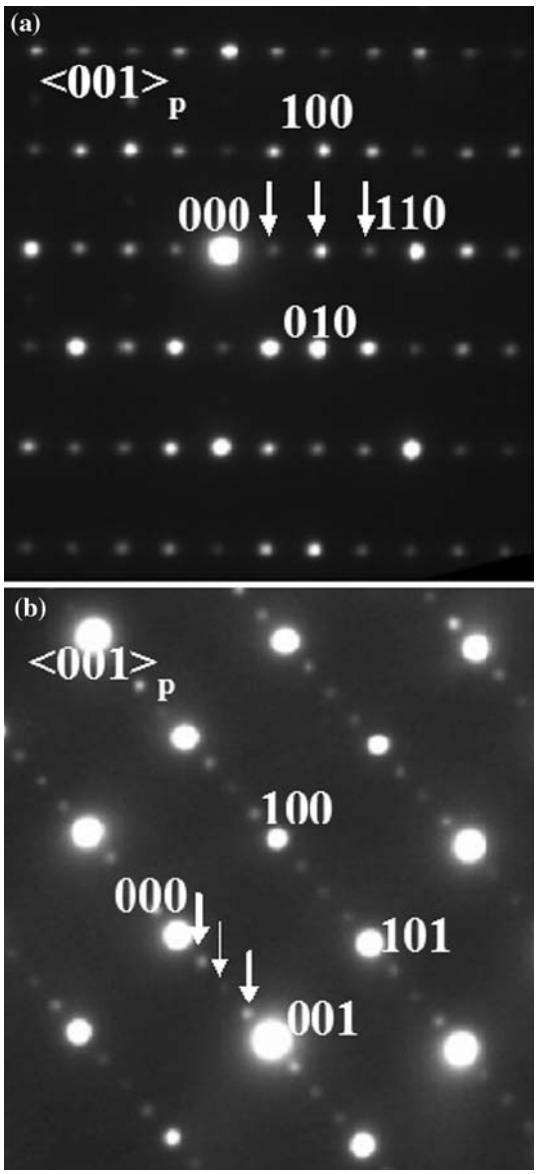

Fig. 10 ED patterns from grains of BNF20 where **a** and **b** are two variants of the $\langle 001 \rangle_p$

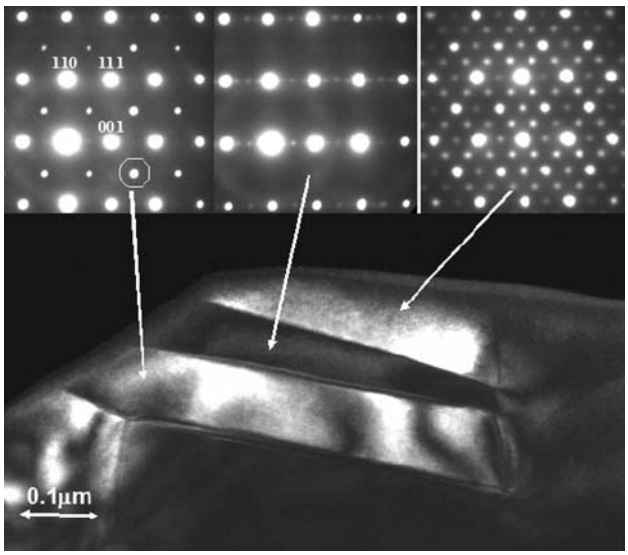

Fig. 11 Domain variance of the pseudocubic $\langle 110 \rangle_p$ direction in BNF20 using $\frac{1}{2}\{ooo\}_p$ superstructure reflection

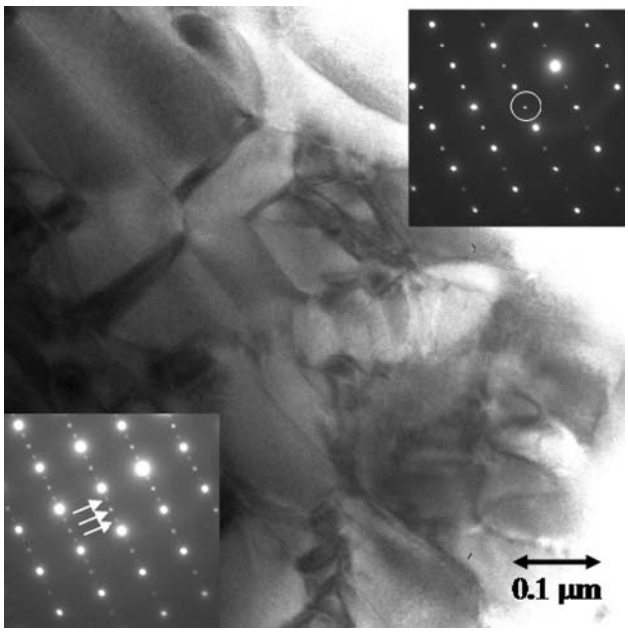

Fig. 12 Room temperature bright field image of a region in BGF12.5 showing mixed $PbZrO_3$-like and orthoferrite phase. Inset are [001] zone axes from each phase. The quadrupled reflections of the $PbZrO_3$-like phase are arrowed and $\frac{1}{2}\{eeo\}$ reflections of the orthoferrite phase are ringed

Raman spectroscopy

Preliminary Raman spectroscopy was also performed as a function of composition and temperature (Figs. 14, 15). No attempt was made to assign modes to the observed bands and the spectra are used in a comparative manner as a means of assessing the onset of structural phase transitions. All spectra broadly followed the same trends as observed in XRD (Fig. 2). For $x \leq 0.1$, all spectra exhibited modes consistent with the rhombohedral, R3c structure of $BiFeO_3$. However, BGF12.5, BNF15, BNF20, BSF15, and BSF17.5 exhibited a similar spectra to each other but markedly different to that of compositions with $x \leq 0.1$. BNF15 and 20 and BSF15 have XRD traces which indicate that they are single-phase of the $PbZrO_3$-like structure. Raman spectra from these samples are therefore considered as characteristic of the new quadrupled cell. BSF17.5 and BNF25 are mixed $PbZrO_3$-like and orthoferrite phase and therefore spectra characteristic of the quadrupled cell are not unexpected. BGF12.5 is on the boundary of transformation from the R3c to orthoferrite cell where the

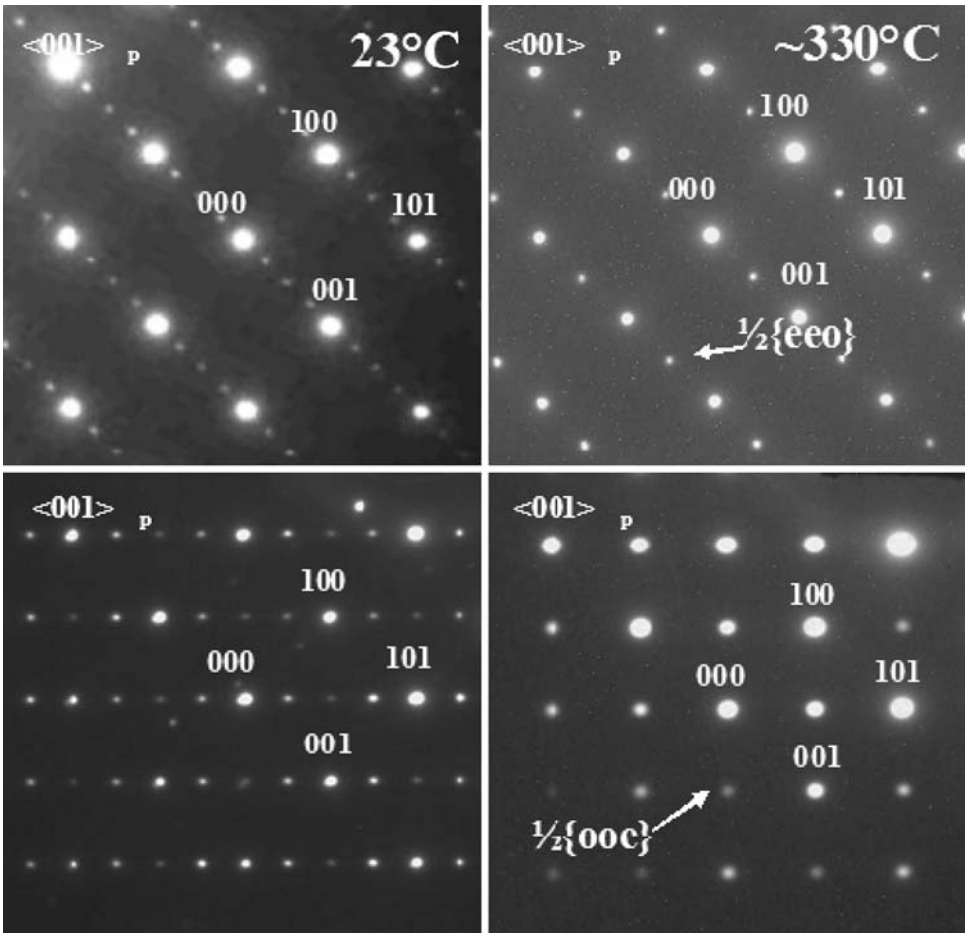

Fig. 13 In situ electron diffraction performed on BNF20 showing the reversible transition from the $PbZrO_3$-like quadrupled cell to an to $a^-a^-c^+$ tilt system

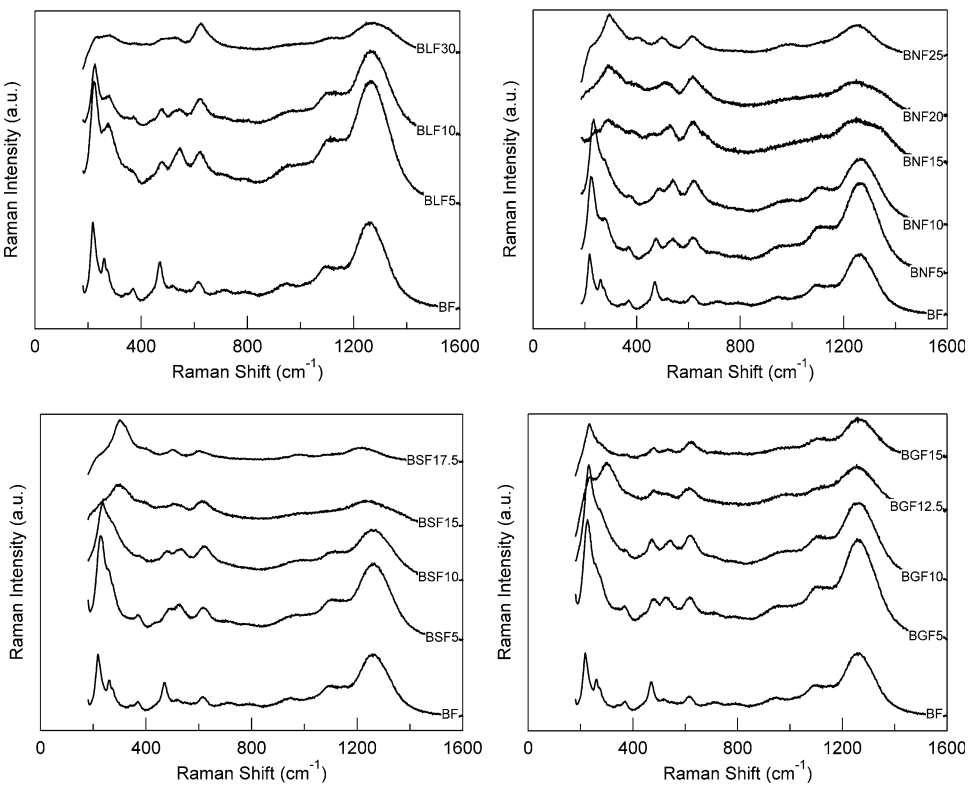

Fig. 14 Raman spectra of BREF100x as a function of composition

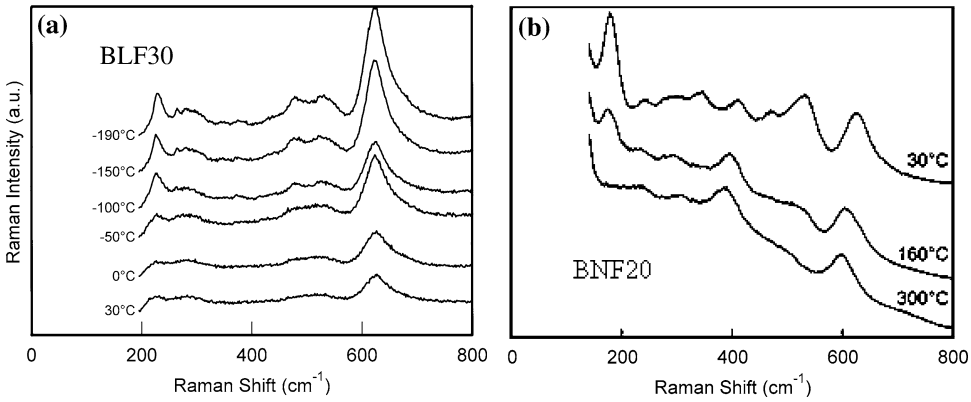

Fig. 15 Raman spectra of BNF20 and BLF30 as a function of temperature

quadrupled phase is known to exist in other RE doped systems. This spectra suggests that it may be possible by use of multiple calcinations to homogeneously distribute the Gd^{3+} to stabilise BGF12.5 as single phase $PbZrO_3$-like structure. BLF30 has a unique trace different to all others which may reflect the pseudocubic nature of the XRD trace for this composition. On cooling BLF30, a further structural phase transition occurs at $\sim$50 °C (Fig. 15a). By analogy with BNF100x and following the tolerance factor and polarizability arguments outlined in the introduction, it is possible that the $PbZrO_3$-like phase is stable in BLF30 below room temperature. Further in situ diffraction is therefore required to determine if BLF30 transforms to the quadrupled cell on cooling. Figure 15b shows the Raman spectra as a function of temperature for BNF20 from 30 to 300 °C. The sharp band at $\sim$180 cm^{-1} disappears at $\sim$200 °C, consistent with the in situ TEM data shown in Fig. 13 in which a structural phase transition is observed over a broad temperature range from the quadrupled $PbZrO_3$-lke to the Pnma, orthoferrite structure.

Discussion

RE doped $BiFeO_3$ compositions have been investigated by many researchers in the last few years and the scientific literature regarding its crystal chemistry is confusing. The general trends presented here shed considerable light on the subject. For all RE doped compositions with $x \leq 0.1$, the R3c cell is favoured at room temperature. For the smaller RE ion, Gd^{3+}, the orthoferrite structure is stabilised for compositions with $x > 0.1$. For the largest RE ion, La^{3+}, the orthoferrite phase is difficult to detect but compositions with $x > 0.2$ showed strong distortions of the high angle XRD peaks which has been attributed to the Pnma cell. For RE ions with intermediate ionic radii, Nd^{3+} and Sm^{3+}, there is a compositional window around $x = 0.15$ within which a new structure is stabilised at room temperature. This phase has a quadrupled unit cell similar to $PbZrO_3$ but with $c = 4a$ rather than $2a$ [26]. On heating, this phase transforms to the orthoferrite structure. The new $PbZrO_3$-like phase forms within a compositional range where there is competition between two tilt systems/structures: $a^-a^-a^-$ and $a^-a^-c^+$ associated with the *R3c*, $BiFeO_3$, and Pnma, orthoferrite end members, respectively. It is proposed that within this narrow window of composition a new tilt system is stabilised through coupling of the octahedral rotations to antipolar rather than polar Bi displacements. The electron diffraction patterns indicate that the tilt system of the new structure is similar to that of $NaNbO_3$ [31] in which the *a* and *b* axes are tilted in antiphase but *c* has a complex modulated in-phase/antiphase tilt system that gives additional multiplication of the unit cell resulting in a periodicity of *4a*. Peaks of varying intensity from the quadrupled $PbZrO_3$-like cell were observed in all solid solutions but only Nd and Sm doped compositions exhibited single phase by XRD The compositional window for which the phase can be stabilised increased with increasing RE ion radius for Gd, Sm and Nd but the largest RE substituent, La^{3+}, did not result in single phase $PbZrO_3$-like phase at room temperature. It is possible that the concentration of La required to induce competition between $a^-a^-a^-$ and $a^-a^-c^+$ tilt systems is so great that there is no longer sufficiently large average A-site polarizability to induce an antipolar state above room temperature. Raman spectroscopy revealed a phase transition at ~ -50 °C for BLF30 but further work is required to clarify if this is the orthoferrite to $PbZrO_3$-like transformation observed in Nd and Sm doped compositions.

Figure 16 show preliminary phase diagrams for the BREF100x system which illustrates concisely many of the points raised above. A general implication of the preliminary phase diagrams is that the orthoferrite, Pnma cell is the high temperature phase for the R3c cell as well as the $PbZrO_3$-like structure unless there are further structural phase transitions on heating for $BiFeO_3$ and compositions close to this end member. However, no further strong

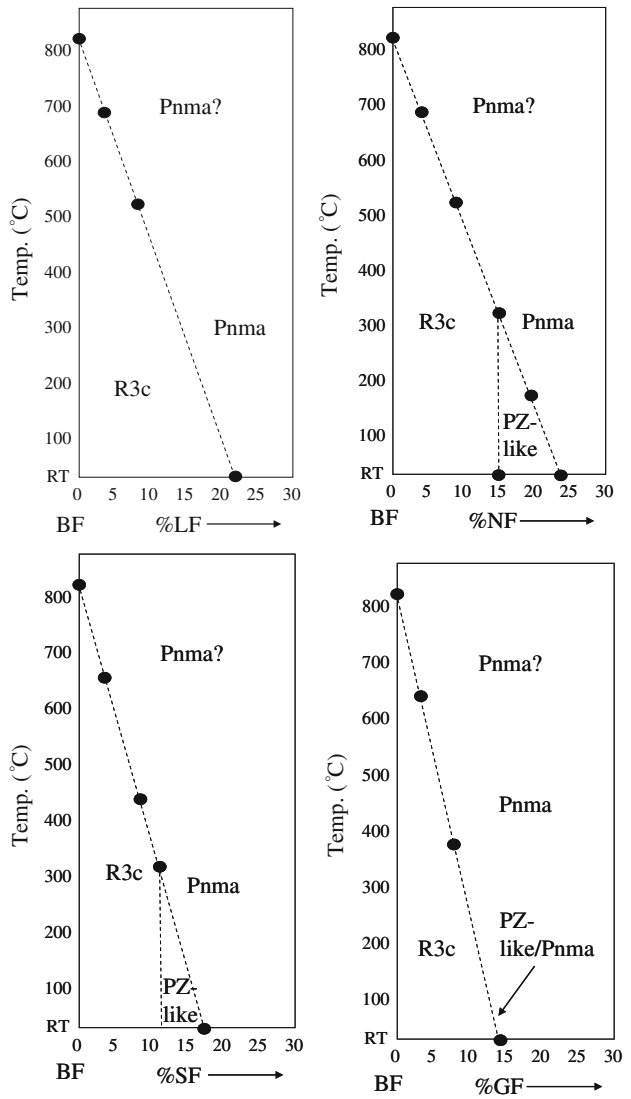

Fig. 16 Preliminary phase diagrams for BRE100x derived using a combination of XRD, DSC, Raman, and TEM data

anomalies were detected by DSC. A paraelectric, Pnma high temperature phase is more logical than initially appears since the tolerance factor for BF and BNF100x are all low enough ($t \leq 0.96$) to stabilise the $a^-a^-c^+$ tilt system to very high temperature [30]. Effectively, when polarisation is absent (i.e. above T_C) the symmetry is dominated by the tilt system which is controlled by the low tolerance factor.

T_C in RE doped Bi ferrites decreased linearly with both average tolerance factor and A-site ionic polarizability. In general, tolerance factor is only a secondary criterion in ferroelectric behaviour unless there is strong coupling to distortions of the octahedral network such as occurs in some Aurivillius phases [32] and $BaRE_2Nb_2Ti_3O_{15}$ tetragonal tungsten bronzes [33]. In each of these cases, ferroelectric order is driven principally by complex rotations of the *O*-octahedra and T_C increases rather than decreases with decreasing tolerance factor/A-site ion radius. It is more likely therefore that the linear relationship of tolerance factor with T_C for RE-doped $BiFeO_3$ is secondary to that with average A-site ionic polarizability, although ionic radius and polarizability are related in the case of RE ions. The values of polarizability were obtained from Shannon [25] but it is evident from the Fig. 7 that the data points for BLF5 and BLF10 are anomalous and do not fit the linear trend. The polarizabilities for Gd^{3+}, Sm^{3+}, Nd^{3+}, La^{3+}, and Bi^{3+} are quoted as 4.37, 4.74, 5.01, 6.07 and 6.12 Å^3, respectively, by the author of Ref. [25]. Within the highly distorted environment of the R3c, ferroelectric cell which is dominated by large A-site ion off centring along [111], a polarizability of 6.07 for La^{3+} seems too large in comparison with Bi^{3+} (6.12 Å^3) and a value of $\sim$5.5 Å^3 is more likely. If this value is assumed then a linear of fit with T_C is obtained for all RE doped compositions (Fig. 7).

Conclusions

(i) A broad overview of the crystal chemistry and domain structure of RE doped $BiFeO_3$ is described.
(ii) All compositions with $x \leq 0.1$ were rhombohedral with R3c symmetry and exhibited superstructure and orientational and translational domains characteristic of an antiphase tilted, ferroelectric perovskite.
(iii) The orthoferrite, Pnma structure was stabilised at lower values of x as the RE ferrite, end member tolerance factor decreased.
(iv) At the phase boundary between the orthoferrite, Pnma cell and rhombohedral, R3c cell in Nd and Sm doped systems, a new structure is stabilised which has a quadrupled unit cell, $\sqrt{2}a$, $2\sqrt{2}a$, $4a$ and is similar to $PbZrO_3$.
(v) On cooling BLF30, a structural phase transition was observed by in situ Raman spectroscopy.
(vi) T_C decreases with decreasing average tolerance factor and A-site ionic polarizability.

Acknowledgements The authors would like to thank Professor C. A. Randall, Professor D.C. Sinclair, and Dr. I. Levin for their useful discussions concerning this manuscript.

References

1. Sosnowska I, Peterlin-Neumaier T, Steichele E (1982) J Phys C: Solid State Phys 15:4835
2. Michel C, Moreau JM, Achenbach GD, Gerson R, James WJ (1969) Solid State Commun 7:701
3. Neaton BJ, Ederer C, Waghmare UV, Spaldin NA, Rabe KM (2005) Phys Rev B Condens Matter Mater Phys 71:014113

4. Teague JR, Gerson R, James WJ (1970) Solid State Commun 8:1073
5. Kumar MM, Palkar VR, Srinivas K, Suryanarayana SV (2000) Appl Phys Lett 76(19):2764
6. Sosnowska I, Prezenioslo R, Fischer P, Murashov VA (1996) J Magn Magn Mater 160:384
7. Fischer P, Polomska M, Sosnowska I, Szymanski M (1980) J Phys C: Solid State Phys 13:1931
8. Kubel F, Schmid H (1990) Acta Crystallogr B46:698
9. Nawala KS, Grag A, Upadhyaya A (2008) Mater Lett 62:878
10. Hill NA (2000) J Phys Chem B24:6694
11. Fedulov SA, Ladyzhinskii PB, Pyatigorskaya IL, Venevtsev YN (1964) Sov Phys Solid State 6:375
12. Yuan GL, Or SW (2006) J Appl Phys 100:024109
13. Fiebig M (2005) J Phys D 38:R123
14. Zhang ST, Zhang Y, Lu MH, Du CL, Chen YF, Liu ZG, Zhu YY, Ming NB (2006) Appl Phys Lett 88:162901
15. Sosnowska I, Schaffer W, Kockelmann W, Anderson KH, Troyanchuk IO (2002) Appl Phys A: Mater Sci Process 74:S1040
16. Bai F, Wang J, Wuttig M, Li J, Wang N, Pyatakov AP, Zvezdin AK, Cross LE, Viehland D (2005) Appl Phys Lett 86(3):1
17. Pradhan AK, Zhang K, Hunter D, Dadson JB, Loutts GB, Bhattacharya P, Katiyar R, Zhang J, Sellmyer DJ (2005) J Appl Phys 97:093903
18. Lee YH, Wu JM, Lai CH (2006) Appl Phys Lett 88(4):042903
19. Das SR, Choudhary RNP, Bhattacharya P, Katiyar RS, Dutta P, Manivannan A, Seehra MS (2007) J Appl Phys 101:034104
20. Yuan GL, Or SW (2006) Appl Phys Lett 89:052905
21. Uniyal P, Yadav KL (2008) Mater Lett 62(17–18):2858
22. Woodward DI (2004) The crystal chemistry of bismuth-based perovskite solid solutions. PhD Thesis, University of Sheffield, UK
23. Jaffe B, Cook WRJ, Jaffe H (1971) Piezoelectric ceramics. Academic Press, London
24. Shannon RD (1976) Acta Crystallogr A32:751
25. Shannon RD (1993) J Appl Phys 73(1):348
26. Karimi S, Reaney IM, Sterianou I, Levin I (2009) Appl Phys Lett 94(11):112903
27. Marezio M, Remeika JP, Dernier PD (1970) Acta Crystallogr B26:2008
28. Sawaguchi E, Maniwa H, Hoshino S (1951) Phys Rev 83(5):1078
29. Woodward DI, Reaney IM (2005) Acta Crystallogr B61:387
30. Reaney IM, Colla EL, Setter N (1994) J Appl Phys 33:3984
31. Glazer AM, Ahtee M, Megaw HD (1972) Acta Crystallogr A28:179
32. Suárez D, Reaney IM, Lee WE (2001) J Mater Res 16(11):3139
33. Levin I, Stennett MC, Miles GC, Woodward DI, West AR, Reaney IM (2006) Appl Phys Lett 89:122908